Journal of
Applied Crystallography

ISSN 0021-8898

Received 3 February 2004
Accepted 28 July 2004

Small-angle neutron and X-ray scattering of dispersions of oleic-acid-coated magnetic iron particles

Karen Butter,[a] Armin Hoell,[b] Albrecht Wiedenmann,[b] Andrei V. Petukhov[a] and Gert-Jan Vroege[a]*

[a]Van 't Hoff Laboratory for Physical and Colloid Chemistry, Debye Institute, Utrecht University, Padualaan 8, 3584 CH Utrecht, The Netherlands, and [b]Hahn-Meitner-Institut Berlin, Glienicker-strasse 100, D-14109 Berlin, Germany. Correspondence e-mail: g.j.vroege@chem.uu.nl

This paper describes the characterization of dispersions of oleic-acid-coated magnetic iron particles by small-angle neutron and X-ray scattering (SANS and SAXS). Both oxidized and non-oxidized dilute samples were studied by SANS at different contrasts. The non-oxidized samples are found to consist of non-interacting superparamagnetic single dipolar particles, with a lognormal distribution of iron cores, surrounded by a surfactant shell, which is partially penetrated by solvent. This model is supported by SAXS measurements on the same dispersion. Small iron particles are expected to oxidize upon exposure to air. SANS was used to study the effect of this oxidation, both on single particles, as well as on interparticle interactions. It is found that on exposure to air, a non-magnetic oxide layer is formed around the iron cores, which causes an increase of particle size. In addition, particles are found to aggregate upon oxidation, presumably because the surfactant density on the particle surfaces is decreased.

1. Introduction

Dispersions of iron particles appear to be very suitable for studying the physical behaviour of ferrofluids. Their synthesis from iron carbonyl compounds results in particles with low polydispersity, of which the particle size can be varied in a controlled way (Butter, 2003; Butter *et al.*, 2003*a*; Papirer *et al.*, 1982). Variation of the iron core size, as well as the thickness of the surfactant layer (by using different types of surfactant) allows control of both the dipolar and isotropic interparticle interaction (Butter, 2003; Butter *et al.*, 2003*b*; Griffiths *et al.*, 1979). In this paper, the characterization of dispersions of iron particles coated with oleic acid using small-angle scattering is described. Dispersions kept under nitrogen atmosphere (to prevent oxidation of the particles), as well as oxidized dispersions were studied. Since the ferrofluids are black, the use of light scattering is difficult due to strong absorbance of visible light. This problem is avoided using small-angle neutron and X-ray scattering (SANS and SAXS). An additional advantage of SANS is the possibility to study the magnetic properties of iron-based particles (Bergenti *et al.*, 2003; Spizzo *et al.*, 2003), since neutron scattering consists of both a nuclear and a magnetic part (see §2). In addition, contrast variation can be used to study different parts of a composite particle by controlled deuteration of the solvent. The theoretical section (§2) summarizes the most important background details concerning scattering, required to understand the experiments; for a more extensive description of SANS and SAXS see the references (Feigin & Svergun, 1987; Glatter & Kratky, 1982; Hayter, 1991; Wiedenmann, 2001). §§3 and 4 describe the scattering experiments and two models that were used to fit the scattering data. In §5, the results are discussed and compared with other experiments on the same dispersions.

2. Theory

2.1. Scattering

The scattering from a dilute dispersion of monodisperse spherical colloids (where particle interactions are assumed to be negligible) as a function of the scattering direction is given by

$$I(\mathbf{q}) = KN_{\rm p}\left|F(\mathbf{q})\right|^2, \tag{1}$$

with $N_{\rm p}$ the number of scattering particles and K a constant, depending on the experimental setup. $F(\mathbf{q})$ is the total scattering amplitude of a single particle,

$$F(\mathbf{q}) = \int_{V_{\rm p}} \Delta\eta(\mathbf{r}) \exp(i\,\mathbf{q}\cdot\mathbf{r})\,{\rm d}\mathbf{r}, \tag{2}$$

which integrates all coherent scattering contributions within the particle of volume $V_{\rm p}$ weighted by their phase shifts $\exp(i\,\mathbf{q}\cdot\mathbf{r})$, with $\mathbf{r}$ the position vector within the particle and $\mathbf{q}$ the scattering vector with magnitude:

$$q = (4\pi/\lambda)\sin(\theta/2). \tag{3}$$

Here, λ is the wavelength of the scattered radiation (equal to that of the incoming beam) and θ the scattering angle between the incident and scattered waves. The local scattering amplitude is quantified as the local scattering length density

difference $\Delta\eta(\mathbf{r})$ with respect to the (homogeneous) solvent scattering length density η_s. ($\Delta\eta$ is also referred to as 'contrast'.)

For spherically symmetric core–shell particles with core radius a_1 with $\Delta\eta = \Delta\eta_1$ and a shell with thickness $(a_2 - a_1)$ and $\Delta\eta = \Delta\eta_2$, the total scattering amplitude of a single particle is given by

$$F(\mathbf{q}) = \int_0^{a_1} \Delta\eta_1 \frac{\sin(qr)}{qr} 4\pi r^2 \,\mathrm{d}r + \int_{a_1}^{a_2} \Delta\eta_2 \frac{\sin qr}{qr} 4\pi r^2 \,\mathrm{d}r$$
$$= \frac{4\pi}{q^3}\left\{\Delta\eta_1 g(qa_1) + \Delta\eta_2[g(qa_2) - g(qa_1)]\right\} \quad (4)$$

with

$$g(x) = \sin x - x\cos x.$$

Note that for a homogeneous spherical particle, $F(\mathbf{q})$ is given by only the first term in equation (4), while the equation can be easily extended to particles with multiple shells. In the case of polydisperse particles, the square of the total scattering amplitude $|F(\mathbf{q})|^2$ in equation (1) has to be averaged with the weight given by their size distribution.

For small values of q, the Guinier approximation is valid, by which the radius of gyration R_g can be derived from the slope of a plot of the logarithm of the intensity against q^2:

$$I(q) = I(0)\exp(-\tfrac{1}{3}R_g^2 q^2). \quad (5)$$

For a spherical particle, the radius of gyration is defined as follows:

$$R_g^2 = \int_0^r 4\pi r^4 \Delta\eta(r)\,\mathrm{d}r \Big/ \int_0^r 4\pi r^2 \Delta\eta(r)\,\mathrm{d}r, \quad (6)$$

which is equal to $\frac{3}{5}a^2$ for a homogeneous sphere of radius a. For polydisperse systems, the particle radius as determined from the Guinier plot, a_G, overestimates the average particle radius, since the larger particles have a higher weight in the scattering intensity $I(q) \propto a^6$. The effective value of the radius of gyration is then given by $R_g^2 = (\langle a^8\rangle/\langle a^6\rangle)$ (Glatter & Kratky, 1982), where the angular brackets denote the averaging over the particle size distribution $P(a)$. For a narrow width of the size distribution, the apparent radius derived from the scattering at low q can be corrected for the relative polydispersity σ, according to (Dhont, 1996)

$$a_G = \langle a_G\rangle\left(1 + \frac{13}{2}\sigma^2\right) \quad \text{with} \quad \sigma^2 = \frac{\langle a_G^2\rangle - \langle a_G\rangle^2}{\langle a_G\rangle^2}, \quad (7)$$

where a_G is the measured radius and $\langle a_G\rangle$ is the number average Guinier radius:

$$\langle a_G\rangle = \int P(a_G) a_G \,\mathrm{d}a_G. \quad (8)$$

Equation (7) is derived from the more general equation valid for narrow size distributions (de Kruif *et al.*, 1988):

$$\langle a^n\rangle = \langle a\rangle^n\left[1 + \frac{n(n-1)}{2}\sigma^2\right]. \quad (9)$$

X-rays and neutrons are scattered by electrons and atomic nuclei present in the sample, respectively. Due to the small wavelengths (<1 nm), the information from scattering of colloidal particles will be found at small angles.

2.2. Small-angle neutron scattering

Neutron scattering from magnetic nanoparticles is caused both by direct interactions of neutrons with the nuclei of atoms within the particles and by interactions between the spins of the neutrons and those of the unpaired electrons in the magnetic particles. This results in two types of neutron scattering: magnetic (M) and nuclear (N). The corresponding scattering amplitudes F_N and F_M for nuclear and magnetic scattering are given by equation (2) with respectively $\Delta\eta = \eta_N - \eta_s$ and $\Delta\eta = \eta_M$. Normal contrast variation only varies η_s, but here we will also vary the contrast by using differently polarized neutrons.

Since only those components of the magnetization $\mathbf{M}$ of the sample perpendicular to $\mathbf{q}$ are effective in magnetic neutron scattering (Hayter, 1991; Pynn, 1992), this leads to a magnetic scattering intensity which depends on the angle α between $\mathbf{q}$ and $\mathbf{M}$. When the particles are completely aligned in an external field $\mathbf{H}$, the intensity in the case of unpolarized neutrons is (Wiedenmann, 2000):

$$I(\mathbf{q}, \alpha) \propto F_N^2 + F_M^2 \sin^2\alpha, \quad (10)$$

giving an anisotropic scattering pattern.

The so-called SANSPOL technique makes use of polarized neutrons by sending them through a polarizer. With a spin-flipper, the polarization direction of the incoming beam can be chosen to be up (+) or down (−). In this case, four scattering processes have to be distinguished, two for conserving the polarization direction (non-spin-flip, ++ and −−) and two where the polarization is reversed (spin-flip, +− and −+). With SANSPOL, the polarization direction after scattering is not analysed; the intensity collected in the detector contains both spin-flip and non-spin-flip contributions and depends on the spin polarization of the incoming neutrons. The respective intensities at high field are given by (Wiedenmann, 2000)

$$I^+(q,\alpha) = \left|F^{++}\right|^2 + \left|F^{+-}\right|^2 = F_N^2 + (F_M^2 - 2F_N F_M)\sin^2\alpha,$$
$$I^-(q,\alpha) = |F^{--}|^2 + \left|F^{-+}\right|^2 = F_N^2 + (F_M^2 + 2F_N F_M)\sin^2\alpha. \quad (11)$$

Note that the average of I^+ and I^- (for non-polarized neutrons) results again in equation (10). At lower magnetic fields, the situation is more complicated since the magnetic moments are no longer completely aligned and their orientation distribution (for non-interacting superparamagnetic particles) follows Langevin statistics (Pynn, 1992; Wiedenmann, 2001). The net alignment of particles in the field direction is given by

$$L(x) = \coth(x) - 1/x \quad (12)$$

where x is proportional to the magnetic moment per particle $\mu = 4\pi a^3 m_s/3$ (m_s is the saturation magnetization per volume) and the magnetic field H:

$$x = \mu_0 \mu H/3kT, \tag{13}$$

with μ_0 the magnetic permeability in vacuum and kT the thermal energy. In this case, the intensities I^+ and I^- are given by (Wiedenmann, 2001):

$$\begin{aligned} I^+(q,\alpha) &\propto F_N^2 + 2F_M^2 L(x)/x + \left\{F_M^2[1 - 3L(x)/x] \right. \\ &\quad \left. - 2F_N F_M L(x)\right\} \sin^2\alpha, \\ I^-(q,\alpha) &\propto F_N^2 + 2F_M^2 L(x)/x + \left\{F_M^2[1 - 3L(x)/x] \right. \\ &\quad \left. + 2F_N F_M L(x)\right\} \sin^2\alpha. \end{aligned} \tag{14}$$

For the case of complete alignment [$L(x \to \infty) = 1$], equation (11) is again obtained. In the limit of zero applied field ($x \to 0$), $L(x)/x \to 1/3$ and the scattering intensity $I^+ = I^- = F_N^2 + 2/3F_M^2$ does not depend on neutron spin polarization and α. As is clear from the above equations (14), $L(x)$ can be derived by subtraction of I^- and I^+ for a certain field value (Wiedenmann, 2001):

$$L(x) = \left(I_x^- - I_x^+\right)/\left(I_{x_\infty}^- - I_{x_\infty}^+\right). \tag{15}$$

Using SANS has the advantage that information about both the 'nuclear' and the 'magnetic' behaviour of particles can be extracted. In this case it is of course necessary to apply a magnetic field to the sample, which might change the particle structure. For polarized neutrons, the two independent scattering patterns for both polarization states are fitted for all q values to the $\sin^2\alpha$ dependency as in equation (11). From the resulting fits, the scattering intensity is calculated for $\alpha = \pi/2(\mathbf{q} \perp \mathbf{H})$:

$$\begin{aligned} I^+(q,\pi/2) &\propto (F_N - F_M)^2, \\ I^-(q,\pi/2) &\propto (F_N + F_M)^2. \end{aligned} \tag{16}$$

Thus, SANSPOL provides an additional method of contrast variation (apart from contrast variation by deuterating the solvent) where the total scattering length density of the (magnetic) core for the different polarization states can be given by $\eta_N + \eta_M$ for (−) and $\eta_N - \eta_M$ for (+), as is employed in Fig. 3 (discussed later). Of course, no magnetic scattering contribution is present for the solvent and non-magnetic parts of the particles, resulting in equal scattering length densities for both the (−) and the (+) polarization states. Another important advantage of polarized neutrons is that due to the presence of the mixing term of both nuclear and magnetic scattering in equation (11), the actual scattering of a composite particle (*e.g.* with a core–shell structure) is measured, whereas measurements with unpolarized neutrons only result in separate magnetic and nuclear size distributions.

2.3. Small-angle X-ray scattering

For SAXS measurements, one can use synchrotron radiation, which is emitted by electrons circulating in a storage ring (Glatter & Kratky, 1982). Although the effect of magnetic order on X-ray scattering is too weak to enable direct access to magnetic properties of the colloidal particles, the SAXS technique has several advantages. The synchrotron X-rays are produced with a much more narrow spectral width ($\Delta\lambda/\lambda \simeq 5 \times 10^{-4}$ for X-rays *versus* about 10% for neutrons used for SANS) as a result of the double-crystal monochromator used for SAXS (Borsboom *et al.*, 1998). Moreover, synchrotron X-rays can be much better collimated thanks to the very small size of the electron beam and a large sample–detector distance. As a result of these factors, the reciprocal-space resolution $\Delta q/q$ is typically a few percent for SAXS, mostly limited by the resolution of the detector, while the poorer resolution of SANS may result in a larger apparent polydispersity of the particles. In addition, the high intensity of the synchrotron X-ray beam permits much faster acquisition of scattering data.

3. Experimental

3.1. Synthesis and characterization of ferrofluid

The iron dispersion OA3 was synthesized under nitrogen atmosphere by thermal decomposition (at 443 K) of $Fe(CO)_5$ in decalin in the presence of oleic acid as described by Butter (2003) and Butter *et al.* (2004*c*). The resulting black dispersion was always stored and handled under nitrogen atmosphere to prevent oxidation of the particles. Part of dispersion OA3 was exposed to air for two days and is further coded as dispersion OA3ox. For further details about the synthesis and characterization the reader is referred to Butter (2003) and Butter *et al.* (2004) (system code OA3).

3.2. Small-angle neutron scattering

Samples for SANS measurements were prepared in a glovebox under nitrogen atmosphere in flat circular quartz cells (Hellma, thickness 0.1 cm). Diluted samples were prepared from the stock dispersion OA3 by adding decalin and/or deuterated decalin to vary the contrast of particles. Sample cells, closed with a cap, were tested to be airtight. Oxidized samples were also prepared in the glovebox (to keep the same level of oxidation for all samples) from the stock dispersion OA3ox.

Measurements were performed at the Berlin Neutron Scattering Centre (BENSC) at the instrument V4 using polarized neutrons (SANSPOL) (Keiderling & Wiedenmann, 1995; Keller *et al.*, 2000) at a wavelength of 0.605 nm with a beam diameter of 16 mm. A schematic setup for measuring SANS can be found at the BENSC instrumentation website (http://www.hmi.de/bensc/instrumentation/instrumente/v4/v4.html). For the SANS instrument V4 installed at the HMI reactor Ber II, the spread in wavelength is rather large ($\Delta\lambda/\lambda \simeq 10\%$) (Keller *et al.*, 2000). Because neutrons at BENSC are produced in a cold source, a relatively high wavelength can be selected, which has the advantage that the scattering angles are not too small (and consequently the sample–detector distance is not too large). Measurements were performed at three different sample–detector distances (1, 4 and 12 m), resulting in a total accessible q range of 0.04 to

3.3 nm^{-1}. The samples were placed between the poles of a strong magnet with the homogeneous magnetic field (up to 1.1 Tesla) in the horizontal direction perpendicular to the beam. Unless stated otherwise, all measurements were performed at maximum field intensity. The neutrons were collected by an ^{3}He detector of 64 × 64 elements of 10 × 10 mm. Measurements were performed on series of different contrasts of dilute samples, both for non-oxidized (∼6.5 times dilution of OA3) and oxidized particles (∼3.3 times dilution of OA3ox). In addition, the non-oxidized stock dispersion and a dilute dispersion were measured under different magnetic field strengths.

Two-dimensional data were corrected for transmission and for background and empty-cell scattering. The sensitivity of individual detector pixels was normalized by comparison with the isotropic scattering of water. The scattering patterns for both polarization states were fitted separately to the $\sin^2\alpha$ fit [as in equation (11)] for all q values. Of the resulting fits, the scattering intensity was calculated for $\alpha = \pi/2$ (for $\mathbf{q} \perp \mathbf{H}$). The curves resulting for the three different sample–detector distances were merged to one curve. Scattering curves were fitted using least-square model fitting computer programs, *FISH* (Heenan, 1998) and *SASFIT* (Kohlbrecher, 2000).

3.3. Small-angle X-ray scattering

SAXS samples were prepared in a glovebox in flat glass capillaries (Vitrocom, internal thickness 1 mm) that were closed with epoxy glue. Measurements were performed at the Dutch–Belgian Beamline (DUBBLE) (Borsboom *et al.*, 1998; Bras, 1998) at the European Synchrotron Radiation Facility (ESRF) in Grenoble, France. The wavelength of the X-ray beam of 0.13 nm (9.5 keV, $\Delta\lambda/\lambda \simeq 5 \times 10^{-4}$) and a sample–detector distance of 1.9 m, resulted in a q range of 0.15–3.2 nm^{-1}. The scattering was collected on a two-dimensional multiwire gas-filled detector, with an area of 13 × 13 cm, containing 512 × 512 pixels.

Two-dimensional data were corrected for transmission, detector sensitivity and background scattering. The two-dimensional patterns were radially averaged.

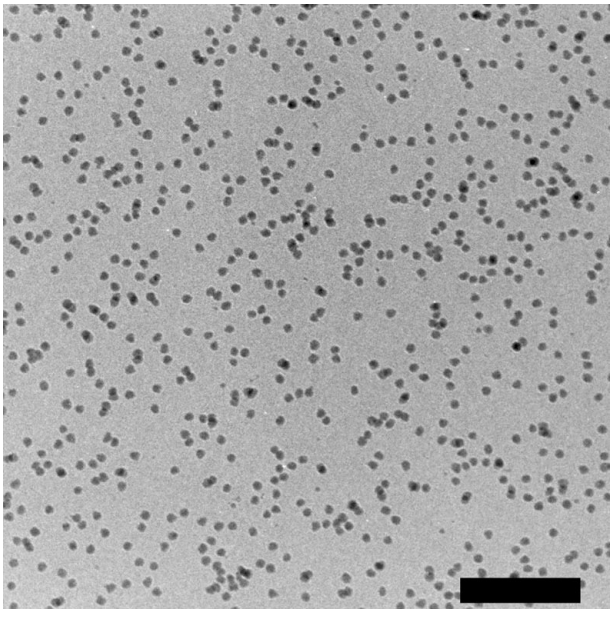

Figure 1
Cryogenic transmission electron microscopy (cryo-TEM) picture of a glassified film of dispersion OA3 showing the iron-based cores. Surfactant layers are not visible with this technique. The scale bar is 100 nm.

Table 1
Characteristics of dispersion OA3.

a_{TEM} (nm)†	4.3 ± 0.3
a_M (nm)‡	3.3
$\varphi_{iron,EA}$§	0.045 (stock)
	0.0070 (non-ox, dilute)
	0.014 (ox, dilute)

† Average particle radius measured from TEM micrographs. ‡ Magnetic particle radius, determined by magnetization measurements (see Fig. 8) using a literature value for m_s of Fe_3C (1.49×10^6 Am^{-1}). § Estimated volume fraction of iron, from elemental analysis of stock dispersion OA3. The value for oxidized particles is calculated assuming that the volume fractions of OA3 and OA3ox are equal (increase of particle size upon oxidation is neglected).

4. Results

4.1. Synthesis and characterization of ferrofluid

The synthesis resulted in a black dispersion that could be manipulated by the field gradient of a small permanent magnet. An electron microscopy picture of the particles is given in Fig. 1. The layer of oleic acid around the particles is invisible on the micrograph. From separate Mössbauer measurements (Butter, 2003; Butter *et al.*, 2004; Goossens *et al.*, 2002), it was found that the particle cores consist of $Fe_{0.75}C_{0.25}$. Upon exposure to air, the particles oxidize, as found by a decrease of the magnetic susceptibility with time. On electron microscopy pictures of oxidized particles (not shown), a layer around a core with different intensity is observed, indicating that an iron oxide layer is formed at the surface of the particles. Characterization of the ferrofluid with various techniques is summarized in Table 1.

4.2. Small-angle neutron scattering

4.2.1. Structure and size distribution. SANS curves for dilute samples with different contrasts are presented in Fig. 2. All (+) and (−) curves could be fitted fairly well with a core–shell model with lognormal distribution (with standard deviation σ) of the iron core radius a_{core}

$$P(a_{core}) = \frac{1}{(2\pi\sigma^2)^{1/2}} \frac{1}{a_{core}} \exp\left\{\frac{-[\ln(a_{core}/\langle a_{core}\rangle]^2}{2\sigma^2}\right\} \qquad (17)$$

with

$$\langle a_{core}\rangle = \int P(a_{core}) a_{core}\, \mathrm{d}a_{core},$$

presented in Fig. 3. For small values, σ is equal to the relative polydispersity of a_{core}:

$$\sigma^2 = \left(\langle a_{core}^2\rangle - \langle a_{core}\rangle^2\right)/\langle a_{core}\rangle^2. \qquad (18)$$

The scattering length density variation shown in Fig. 3 clearly revealed a partial penetration of the solvent into the complete

region of the oleic acid shell. Without this feature, the scattering curves could not be fitted consistently. The partial penetration resulted in a homogeneous scattering length density of the surfactant layer in between those of oleic acid and the solvent (see Table 2 and Fig. 3). Note that we used equal parameters (Table 2) in our model, to fit the entire set of data for various contrasts and spin configurations (except for a slight difference in the volume fraction for samples at different contrasts, which can arise from small experimental errors in the concentration).

Fig. 4 shows that the SANS Guinier curve for a dilute sample of non-oxidized particles is nearly straight and from the slope a radius of gyration R_g of 2.9 nm is calculated, corresponding to a particle core radius a_G of 3.8 nm.

The curves of the oxidized particles could not be fitted with one distribution for the whole q range, since the intensity strongly increases at low q (Fig. 5). At higher q (> 0.25 nm^{-1}) curves could be reasonably well fitted with a core–2shell model with a lognormal distribution of the core size, and again a partial penetration of solvent in the oleic acid shell. Here, we used the same contrasts as for the non-oxidized samples for the core and the oleic acid layer and a different contrast to account for an extra iron oxide layer around the core (Figs. 5 and 6). Again, we used equal model parameters for the entire data set. An additional contribution of aggregates was needed

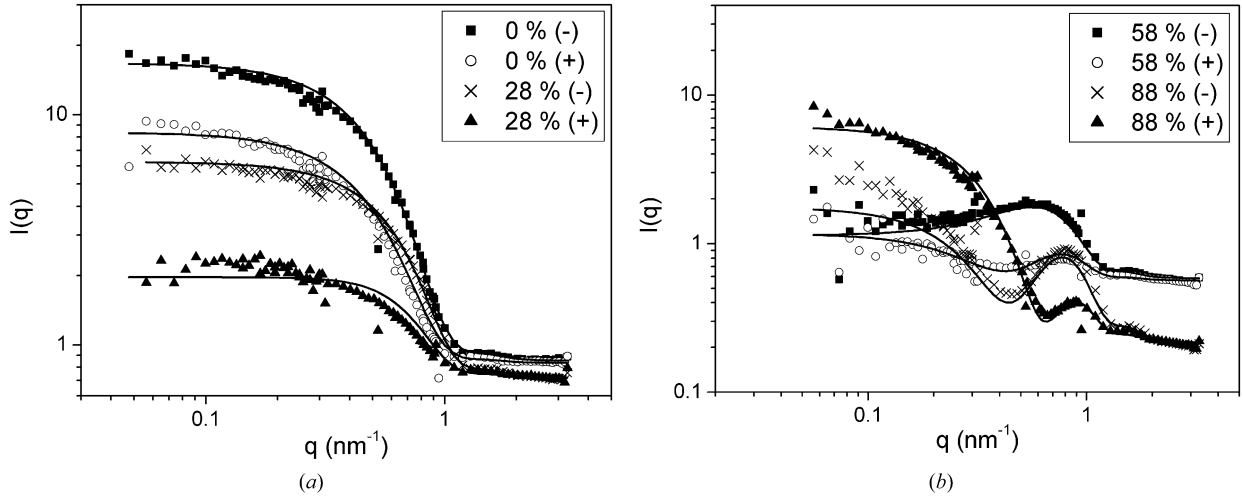

(*a*) (*b*)

Figure 2
SANS scattering curves of dispersion OA3 for different compositions of the solvent (the volume percentage of deuterated decalin is indicated). Both the curves measured with spin up (+) and spin down (−) are shown. The solid curves are fits according to a core–shell model with partial penetration of solvent in the surfactant shell. The fitting parameters can be found in Table 2.

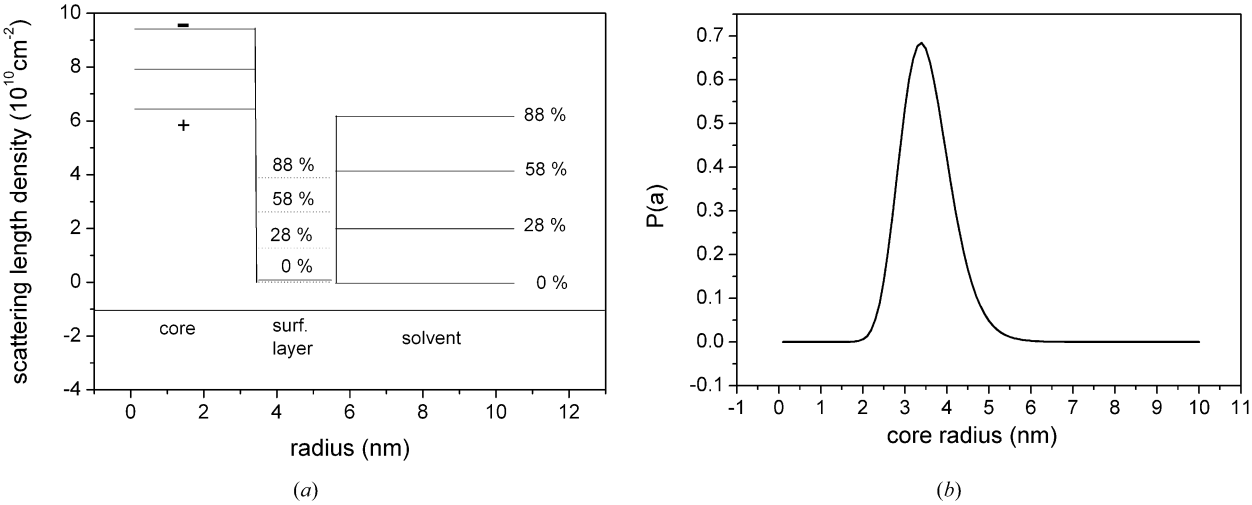

(*a*) (*b*)

Figure 3
(*a*) Core–shell model used to fit SANS curves for dispersion OA3. The dotted lines indicate the average scattering length densities of the surfactant layer (partially penetrated by solvent) for the various amounts of deuteration of the solvent. The fraction of solvent penetrated in the surfactant shell is given by the factor x (about 0.6, see Table 2). The scattering length density of the surfactant shell is an average of oleic acid and solvent and is given by η_N(shell) $= (1 - x)0.08$ (cm^{-2}) $+ x\eta_s$. For the (−) curves, the magnetic and nuclear scattering length densities were added, while for the (+) curves, the magnetic scattering length density was subtracted from the nuclear scattering length density. (*b*) Distribution of the core radius as used in our model.

to fit the curves well for the whole q range. However, this fit contribution very much depends on the exact parameters chosen and we have no information about the exact size, shape and distribution of the aggregates from other techniques. It appeared that the scattering intensity at lower q values could be properly fitted by an additional contribution of larger polydisperse particles (a = 8.3 nm, lognormal distribution with σ = 0.52), which practically does not influence the intensity at higher q values. This point will be discussed further in §5.

The Guinier plot of oxidized particles (Fig. 7) shows a strong steep upturn at low q, indicating the presence of aggregates. However, at slightly higher q values, the dispersion displays clearly Guinier behaviour with a radius of gyration of 3.2 nm, while it is calculated to be 3.1 nm from equation (6), using the fitting parameters of the core–2shell model.

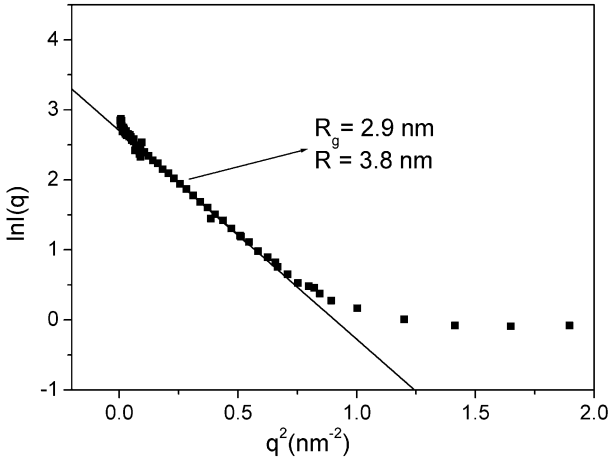

Figure 4
Guinier plot from SANS measurements on dilute dispersion OA3 in 0% deuterated decalin.

Table 2
Fitting parameters for SANS curves of dilute dispersions OA3 and OA3ox.

	OA3		OA3ox	
$\langle a_{core}\rangle$ (nm)†	3.48		2.74	
dR_{shellA} (nm)‡	–		1.37	
dR_{shellB} (nm)‡	2.08		2.08	
η_N(core) (10^{10} cm^{-2})§	7.92		7.92	
η_N(shellA) (10^{10} cm^{-2})§	–		7.29	
η_N(shellB) (10^{10} cm^{-2})§	0.08 (without solvent penetration)		0.08 (without solvent penetration	
	0.01 (0% D)¶		0.02 (0% D)¶	
	1.27 (28% D)¶		1.05 (25% D)¶	
	2.61 (58% D)¶		2.02 (50% D)¶	
	3.88 (88% D)¶		3.05 (75% D)¶	
η_M (10^{10} cm^{-2})††	1.49	1.49		
η_s (10^{10} cm^{-2})§	0% D	−0.031	0% D	−0.031
	∼28% D	1.99	∼25% D	1.81
	∼58% D	4.13	∼50% D	3.54
	∼88% D	6.16	∼75% D	5.37
x‡‡	0.625		0.562	
φ(core)§§	7.0×10^{-3} (0% D and 28% D)		2.7×10^{-3}	
	7.4×10^{-3} (58% D and 88% D)			
σ¶¶	0.170		0.147	

† Average radius of the iron core. ‡ Thickness of the oxide layer (shell A) and the surfactant layer (shell B). § Nuclear scattering length density of the iron core (core), oxide layer (shell A), surfactant layer (shell B), and solvent (for different contrasts). ¶ Calculated from x: η_N(shellB) = (1 − x)0.08 + $x\eta_s$. †† Magnetic scattering length density of the iron core. ‡‡ Fraction of the surfactant layer penetrated by solvent. §§ Volume fraction of iron cores from the absolute intensity of the scattering. ¶¶ Relative polydispersity of iron cores.

4.2.2. Langevin behaviour. The Langevin behaviour of the non-oxidized particles as a function of magnetic field is calculated using equation (15) (Fig. 8). Both curves [from the stock dispersion OA3 and a dilute dispersion (88% deuterated)] are very similar to the normalized magnetization curve of the same stock dispersion, which can be fitted properly to the Langevin function, resulting in a particle dipole moment of

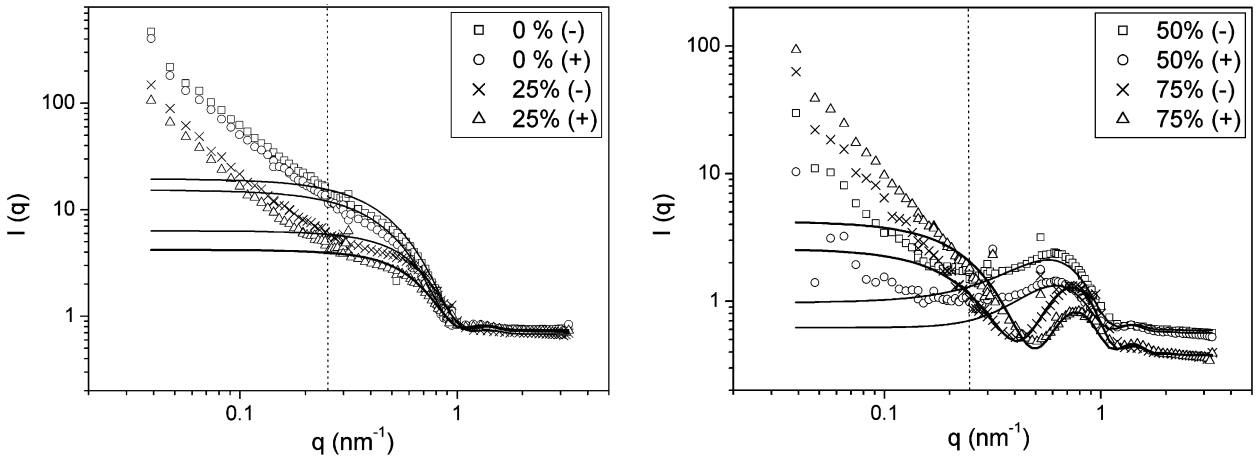

(*a*) (*b*)

Figure 5
SANS scattering curves of dispersion OA3ox for different compositions of the solvent (the volume percentage of deuterated decalin is indicated). Both the curves measured with spin up (+) and spin down (−) are shown. The solid curves are fits according to a core–2shell model with partial penetration of solvent in the surfactant shell. The experimental data were only fitted for $q > 0.25$ nm^{-1} (on the right side of the dotted lines). The fitting parameters can be found in Table 2.

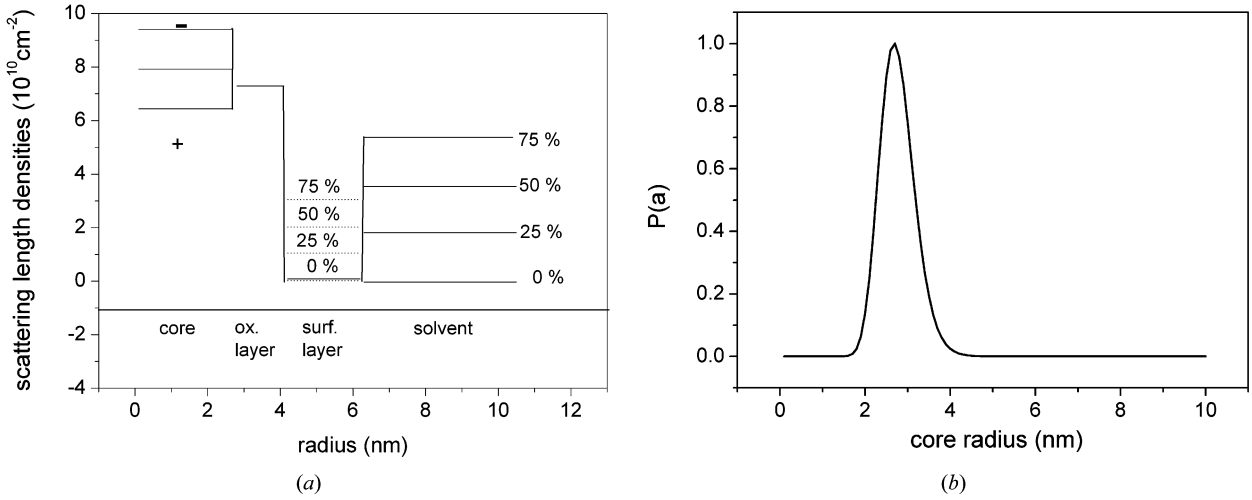

(*a*) (*b*)

Figure 6
(*a*) Core–2shell model used to fit SANS curves for dispersion OA3ox. For further explanation see the caption of Fig. 3. (*b*) Distribution of the core radius as used in our model.

2.24×10^{-19} Am^2 corresponding to a particle radius of 3.3 nm (using a value of 1.49×10^6 Am^{-1} for the saturation magnetization of amorphous $Fe_{0.75}C_{0.25}$; see Table 1). This point will be discussed further in §5. It must be noted that the magnetization curve is much more accurate than the results from SANS, and it consists of many more measuring points. The good agreement between SANSPOL and magnetization results for both the stock and dilute dispersion again indicates the absence of aggregates in the non-oxidized samples.

4.3. Small-angle X-ray scattering

SAXS curves of dilute samples of OA3 only show scattering from the iron cores, since the contrast of the oleic acid layer compared to the solvent can be neglected. Fig. 9 shows a curve of a dilute dispersion (50 times more dilute compared with the stock dispersion) that can be fitted reasonably well with the same particle radius as for the SANS curves (Table 2) and a slightly smaller polydispersity ($\sigma = 0.14$ instead of 0.17). Since for SAXS no absolute intensities are measured, the contrast and particle concentration cannot be compared to the values found for SANS. The radius of gyration found from the SAXS curve is 3.0 nm, corresponding to a Guinier particle radius of 3.9 nm.

5. Discussion

5.1. Non-oxidized ferrofluids

The parameters for the particle radius and volume fraction used for fitting the SANS curves of the non-oxidized samples agree well with information from other techniques (see Tables 1 and 2). The polydispersity found from SANS (17%, Table 2) is significantly larger than is found from TEM measurements

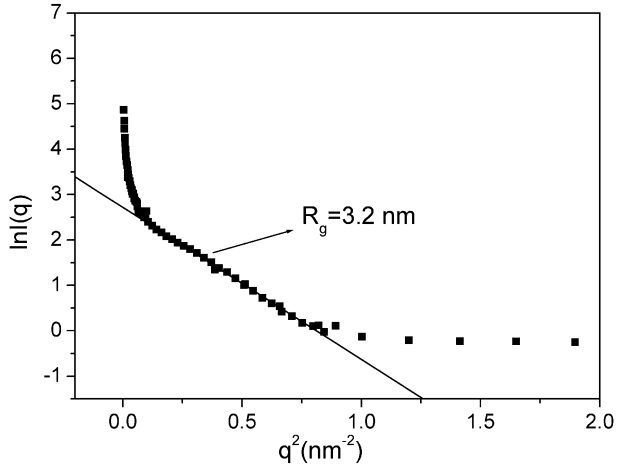

Figure 7
Guinier plot from SANS measurements on dilute dispersion OA3ox in 0% deuterated decalin.

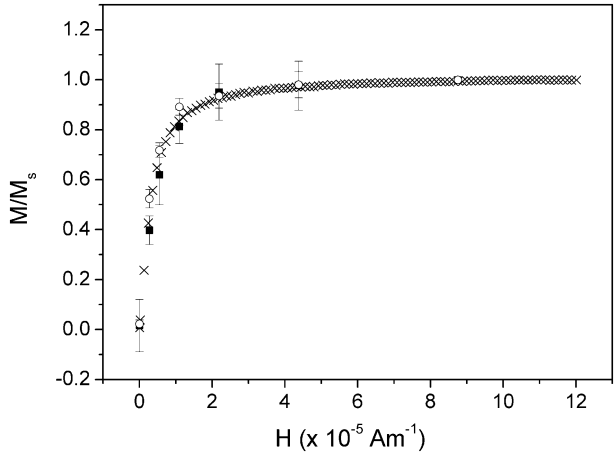

Figure 8
Langevin curves for dispersion OA3: (squares) SANS measurements on stock dispersion, (circles) SANS measurements on dilute dispersion (88% deuterated decalin), (crosses) magnetization curve of stock dispersion.

(7%, Table 1). The apparent polydispersity can be partly caused by smearing of the scattering pattern due to the large distribution in the wavelength of neutrons ($\Delta q/q \simeq \Delta\lambda/\lambda \simeq$ 10%). The SAXS data suggest a somewhat smaller polydispersity (14%), although still much larger than found from TEM. In spite of the much narrower spectral width ($\Delta\lambda/\lambda \simeq 10^{-4}$) of X-rays, which does not limit the resolution $\Delta q/q$, other factors like the finite detector resolution and the finite transverse coherence length (Petukhov *et al.*, 2002) restrict the actual resolution $\Delta q/q$ to a few percent. Thus, although the resolution in SAXS measurements is better than for SANS, it is also limited and SAXS may overestimate the polydispersity as well. On the other hand, TEM is probably less sensitive for smaller particles, which are sometimes neglected when determining the average particle radius, resulting in a slight underestimation of the polydispersity.

The particle radii found from both Guinier plots (respectively 3.8 and 3.9 nm for SANS and SAXS) are somewhat larger than the average particle radius used in our model. However, these values should be corrected for polydispersity (0.14 from SAXS) using equation (7) to obtain the average radii. This results in particle radii of 3.4 nm and 3.5 nm for SANS and SAXS respectively, both very close to the value of 3.48 nm from the model. The thickness of the oleic acid layer (2.08 nm) used in our model is in agreement with the value that is normally used in the literature for other oleic-acid-coated ferrofluids (van Ewijk *et al.*, 2002; Wiedenmann, 2002). In our model, the fraction x of solvent penetration into the oleic acid shell (taking the theoretical value of 0.08×10^{10} cm^{-2} for the scattering length density of pure oleic acid) was found to be 0.62. Note that other authors did not find a partial penetration of solvent in the $C_{21}H_{39}NO_3$ surfactant layers of cobalt particles (Wiedenmann, 2000, 2001). From our fits it appeared that an equal fraction of solvent throughout the whole surfactant layer is a better model than a linear gradient of solvent penetration, where the fraction of solvent is larger at the outside of the surfactant layer. From the fraction of solvent penetration x in the surfactant shell, a rough estimation of the fraction of core surface coverage φ by oleic acid of 0.66 can be made, using the core radius $a_{\rm core}$ (3.48 nm) and thickness of the oleic acid layer L (2.08 nm) as found from the model, and assuming that the surfactant molecules are straight cylinders:

$$\varphi = (x-1)\frac{1-(1+L/a_{\rm core})^3}{3L/a_{\rm core}}. \qquad (19)$$

With a cylinder radius equal to an aliphatic C—H bond length of about 1.5 Å, the value corresponds to a packing density of about 2.3 oleic acid molecules per nm^2, which is significantly lower than is found for oleic-acid-coated magnetite particles [$\sim$3.6 nm^{-2} (van Ewijk *et al.*, 1999)].

The nuclear scattering length density of the core found in the model (7.9×10^{10} cm^{-2}) lies slightly lower than the theoretical value for pure iron [8.1×10^{10} cm^{-2} (Shen *et al.*, 2001)] and lower than the value for $Fe_{0.75}C_{0.25}$, estimated to be 8.9×10^{10} cm^{-2} using a density of 7.58 g ml^{-1} (Bauer-Grosse & Caër, 1987). It should be noted that this last value may not be very accurate, since our particles consist of amorphous material, for which the carbon content and the density could only be estimated (Goossens *et al.*, 2002). The magnetic scattering length density from our model (1.49×10^{10} cm^{-2}) is significantly lower than for α-iron [4.6×10^{10} cm^{-2} (Shen *et al.*, 2001)], which is surprising. For our particles, where the nuclear scattering length density is 7.9/8.9 = 0.888 times lower than the theoretical value for Fe_3C and the magnetic scattering length is 1.49/4.6 times lower than for α-iron, the saturation magnetization can be calculated to be 1.49/(0.888 × 4.6) = 0.36 times the value for α-iron [1.71×10^6 Am^{-1} (Jiles, 1995)], resulting in a value of 0.62×10^6 Am^{-1}. This value is much smaller than the literature value for Fe_3C (1.49×10^6 Am^{-1}) that was used to calculate the magnetic particle radius $a_{\rm M}$ in Table 1 from the average magnetic moment obtained from the Langevin curve. Using the calculated value of $m_{\rm s} = 0.62 \times 10^6$ Am^{-1} to determine $a_{\rm M}$ instead, a larger radius of 4.4 nm is obtained. For polydisperse particles, the value obtained for $a_{\rm M}$ from a Langevin curve is somewhat higher than the number average value $\langle a_{\rm M}\rangle$, since it equals $(\langle a_{\rm M}^6\rangle/\langle a_{\rm M}^3\rangle)^{1/3}$ (Berkovski & Bashtovoy, 1996). After correction for polydispersity (using equation (9) with $\sigma = 0.14$, from SAXS) a value for $\langle a_{\rm M}\rangle$ of 4.0 nm is obtained. Unexpectedly, this radius is larger than the radius found from our fitting model (3.48 nm), while usually the magnetic radius is somewhat smaller than the physical radius owing to the presence of a non-magnetic surface layer (Rosensweig, 1985; Lembke *et al.*, 1999).

Although the fits for non-interacting particles agree fairly well with our experimental data, some effect of the magnetic field on the particle structure was observed in SAXS measurements on dilute samples of the same concentration as used for SANS, showing a different intensity in the horizontal and vertical direction at low q (<0.45 nm^{-1}, up to about 25% difference at the lowest q value of 0.15 nm^{-1}). However, this effect does not seem to be very strong, as the particles show Langevin behaviour of single-domain non-interacting dipoles

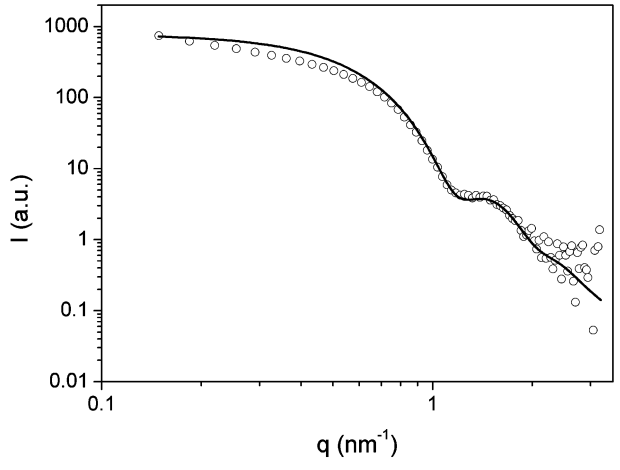

Figure 9
SAXS curve of dilute dispersion OA3. The solid curve is a fit, using the same core radius and a slightly lower polydispersity (0.14) as for the model in Fig. 3.

(Fig. 8), from which a particle size was determined (4.0 nm) that still corresponds reasonably well with that of single particles.

5.2. Oxidized ferrofluids

When the same particles are exposed to air, an oxidized layer is formed at the surface of particles of approximately 1.4 nm. The total particle size (core + oxide shell = 4.1 nm) is significantly larger than for the non-oxidized core (3.5 nm), most probably because the density of the oxidized layer is lower than before oxidation. Increase of the particle size upon oxidation was also found from separate SAXS measurements on a similar dispersion and from measurements of particle sizes on TEM micrographs (Butter, 2003; Butter *et al.*, 2004). From the fit parameters of the oxidized and non-oxidized particles, it can be calculated that the volume of the oxidized layer has increased by a factor of 2.3 due to oxidation. This is in reasonable agreement with what is expected for conventional iron oxides (*e.g.* a factor of 2.1 for transforming Fe into Fe_3O_4). As expected, the scattering contrast of the oxide layer is somewhat lower than for non-oxidized iron (see Table 2). In addition, no magnetic scattering is present from the oxide layer, indicating that a non-ferromagnetic oxide has been formed. This is in agreement with measurements on similar dispersions of the magnetic susceptibility upon oxidation, showing such a large decrease with time, that formation of a magnetic oxide is not very plausible (Butter, 2003; Butter *et al.*, 2004).

There are important indications that oxidation decreases the colloidal stability of the particles. As mentioned earlier, the scattering curves for oxidized dispersions could not be fitted properly at low q values without an additional contribution of clusters, since all curves showed a steep upturn in this region (Fig. 5, left side of dotted line), which is a clear sign of aggregates. Also, the Guinier plot for the oxidized system is extremely steep at low q values (Fig. 7), giving a radius of gyration of many times the single particle value. However, the radius of gyration of single particles can still be determined from a Guinier fit at slightly higher q values (Fig. 7); this R_g (3.2 nm) corresponds well with the value that is expected from the fitting parameters for the oxidized particles [3.1 nm, using equation (6)]. Presumably, the decrease in surfactant density (scaling with a^{-2}, in our case with a factor of 1.4) due to increase of the particle radius upon oxidation, destabilizes some particles, resulting in aggregation. Whereas the scattering curves (Fig. 5) at higher q values ($> 0.25\ \mathrm{nm}^{-1}$) can be fitted with a model of single core–2shell particles (see §4), an additional contribution of aggregates is needed to fit the curves well for the entire q range.

A contribution of spherical aggregates (a = 8.3 nm, lognormal distribution with σ = 0.52) of a homogeneous scattering length density fits our data at lower q range reasonably well, without affecting the fit at higher q values. Since the fitting values for φ and η of the aggregates are dependent on each other and are not known from other techniques, it is not possible to obtain information about the composition and concentration of the aggregates. Concerning this it should be mentioned that the volume fraction of single particles in the model we used for oxidized particles (for $q > 0.25\ \mathrm{nm}^{-1}$) is significantly smaller than is expected from the value for elemental analysis (Table 1). Note that this is partly due to the fact that in our model solely the size of the non-oxidized cores is incorporated in the value for φ. From the discrepancy left after correction of φ for the above effect (with approximately a factor of 2), one could theoretically derive the volume fraction of aggregates in the oxidized dispersion, assuming that the total volume fraction of aggregates and single particles is equal to the value derived from elemental analysis. However, for our fitting contribution of spherical aggregates ($q < 0.25\ \mathrm{nm}^{-1}$), this then yields a value for η ($\sim 1.5 \times 10^{10}\ \mathrm{cm}^{-2}$) that is much lower than would be expected from aggregates of iron particles coated with oleic acid. Probably, larger aggregates that sedimented to the bottom of the container were also present in the dispersion of oxidized particles, resulting in an apparently lower concentration from the SANS measurements.

Apart from a contribution of homogeneous spherical aggregates, the scattering at low q values could also result from the presence of fractal aggregates, where the average scattering length density of the cluster decreases from the centre to the edge of the cluster. From the decay of the scattered intensity, which follows a power law as $\sim q^{-n}$ with $n \simeq$ 1.7–2, a fractal dimension of clusters of about 1.7–2 could be derived. It must be stressed here that various models for contributions of aggregates could be used to fit our data. From the scattering curves only, it will not be possible to find a unique model for the aggregates present in the sample. However, despite the fact that the exact composition, shape and concentration of clusters cannot be derived from the curves, it is clear that the contribution of aggregates does not influence the fits at higher q values, indicating that the scattering curves can be treated as consisting of two separate parts; at high q the scattering results from single core–2shell particles, whereas the intensity at lower q arises from scattering of aggregates.

6. Conclusions

The internal structure of oleic-acid-coated iron particles in ferrofluids was derived by SANS and SAXS measurements. Our particles can be modelled by non-interacting core–shell particles with a lognormal distribution of the iron cores and partial penetration of the surfactant shell by the solvent. The particle sizes, volume fraction of particles and scattering length densities correspond well with those expected from theory and other experimental techniques. On the basis of our model, the packing density of oleic acid on the particle surface was estimated to be 2.3 molecules nm^{-2}. Accurate fitting of the data with our model shows that the dilute ferrofluids consist of superparamagnetic dipoles, where interparticle interaction is negligible. This picture is confirmed by the Langevin behaviour of the particles, as found from both SANS and magnetization measurements. Unexpectedly, the value

found from SANS for the saturation magnetization of our particles was found to be significantly lower than the literature value for Fe_3C. However, this finding should be considered with some reservation since it results in a magnetic particle size that is somewhat larger than the physical particle size found from scattering. Upon exposure to air, particles are found to oxidize. This results in a non-magnetic oxidized layer around the particles, which causes the total particle radius to increase due to decrease of the mass density. Particles do not oxidize completely, since a non-oxidized core still exists, probably due to the passivating iron oxide layer. Oxidation also causes aggregation of the particles, presumably because of decrease of the surfactant density at the particle surface. Although it is not possible to find a unique model describing the exact size, shape and composition of the aggregates, SANS curves of dispersions of oxidized particles could be treated as consisting of two separate parts, which could be fitted by a core–2shell model of single particles ($q > 0.25\ \mathrm{nm}^{-1}$), including a contribution of aggregates ($q < 0.25\ \mathrm{nm}^{-1}$).

Martin Kammel of BENSC is greatly thanked for his help with the analysis of the SANS data. This work was supported by the European Union under Human Potential Program HPRI-CT-2001-00138. Financial support was also granted by the Dutch Technology Foundation (STW) with financial aid from the Council for Chemical Science of the Netherlands Organization for Scientific Research (CW/NWO).

References

Bauer-Grosse, E. & Le Caër, G. (1987). *Philos. Mag. B*, **56**, 485–500.
Bergenti, I., Deriu, A., Savini, L., Bonetti, E. & Hoell, A. (2003). *J. Appl. Cryst.* **36**, 450–453.
Berkovski, B. & Bashtovoy, V. (1996). Editors. *Magnetic Fluids and Applications Handbook*. New York: Begel House.
Borsboom, M., Bras, W., Cerjak, I., Detollenaere, D., Glastra van Loon, D., Goedtkindt, P., Konijnenburg, M., Lassing, P., Levine, Y. K., Munneke, B., Oversluizen, M., van Tol, R. & Vlieg, E. (1998). *J. Synchrotron Rad.* **5**, 518–520.
Bras, W. (1998). *J. Macromol. Sci.-Phys. B*, **37**, 557–565.
Butter, K. (2003). PhD thesis, University of Utrecht, the Netherlands (http://laurel.library.uu.nl/cgi-bin/mus212/dialogserver?DB=da_en.)
Butter, K., Bomans, P. H., Frederik, P. M., Vroege, G. J. & Philipse, A. P. (2003*a*). *Nature Mater.* **2**, 88–91.
Butter, K., Bomans, P. H., Frederik, P. M., Vroege, G. J. & Philipse, A. P. (2003*b*). *J. Phys. Condens. Matter*, **15**, S1451.
Butter, K., Kassapidou, K., Vroege, G. J. & Philipse, A. P. (2004). *J. Colloid Interface Sci.* Submitted.
Dhont, J. K. G. (1996). *An Introduction to Dynamics of Colloids*. Amsterdam: Elsevier.
Ewijk, G. A. van, Vroege, G. J. & Kuipers, B. W. M. (2002). *Langmuir*, **18**, 382–390.
Ewijk, G. A. van, Vroege, G. J. & Philipse, A. P. (1999). *J. Magn. Magn. Mater.* **102**, 31.
Feigin, L. A. & Svergun, D. I. (1987). Editors. *Structure Analysis by Small-Angle X-ray and Neutron Scattering*. New York: Plenum Press.
Glatter, O. & Kratky, O. (1982). Editors. *Small-Angle X-ray Scattering*. New York: Academic Press.
Goossens, A., de Jongh, L. J., Butter, K., Philipse, A. P., Craje, M. W. J. & van der Kraan, A. M. (2002). *Hyperfine Interactions*, **141–142**, 381–386.
Griffiths, C. H., O'Horo, M. P. & Smith, T. W. (1979). *J. Appl. Phys.* **50**, 7108–7115.
Hayter, J. B. (1991). *J. Chem. Soc. Faraday Trans.* **87**, 403–410.
Heenan, R. K. (1998). Report 89–129, ISIS Department, Rutherford Appleton Laboratory, Oxon, UK.
Jiles, D. (1995). *Introduction to Magnetism and Magnetic Materials*. London: Chapman and Hall.
Keiderling, U. & Wiedenmann, A. (1995). *Physica B*, **213–214**, 895–897.
Keller, T., Krist, T., Danzig, A., Keiderling, U., Mezei, F. & Wiedenmann, A. (2000). *Nucl. Instrum. Methods Phys. Res. A*, **451**, 474–479.
Kohlbrecher, J. (2000). *SASFIT*. Berlin Neutron Scattering Centre (BENSC).
Kruif, C. G. de, Briels, W. J., May, R. P. & Vrij, A. (1988). *Langmuir*, **4**, 668–676.
Lembke, U., Hoell, A., Kranold, R., Muller, R., Schuppel, W., Gilles, R. & Wiedenmann, A. (1999). *J. Appl. Phys.* **85**, 2279–2286.
Petukhov, A. V., Aarts, D. G. A. L., Dolbnya, I. P., de Hoog, E. H. A., Kassapidou, K., Vroege, G. J., Bras, W. & Lekkerkerker, H. N. W. (2002). *Phys. Rev. Lett.* **88**, 208301.
Papirer, E., Horny, P., Balard, H., Anthore, R., Petipas, C. & Martinet, A. (1982). *J. Collect. Int. Sci.* **94**, 207–219.
Pynn, R. (1992). *Probing Fine Magnetic Particles with Neutron Scattering. Studies of Magnetic Properties of Fine Particles and their Relevance to Materials Science*, edited by J. L. Dormann & D. Fiorani, pp. 287–296. Amsterdam: Elsevier.
Rosensweig, R. E. (1985). *Ferrohydrodynamics*. Cambridge University Press.
Shen, L., Stachowiak, A., Fateen, S. K., Laibinis, P. E. & Hatton, T. A. (2001). *Langmuir*, **17**, 288–299.
Spizzo, F., Angeli, E., Bisero, D., Da Re, A., Ronconi, F., Vavassori, P., Bergenti, I., Deriu, A. & Hoell, A. (2003). *J. Appl. Cryst.* **36**, 826–828.
Wiedenmann, A. (2000). *J. Appl. Cryst.* **33**, 428–432.
Wiedenmann, A. (2001). *Physica B*, **297**, 226–233.
Wiedenmann, A. (2002). *Lecture Notes on Physics*, edited by S. Odenbach, pp. 33–58. Berlin: Springer.